Article

Polydopamine-Bi$_2$WO$_6$-Decorated Gauzes as Dual-Functional Membranes for Solar Steam Generation and Photocatalytic Degradation Applications

Yea-Chin Wang [1], Chi-Jung Chang [1,*], Chih-Feng Huang [2], Hao-Cheng Zhang [1] and Chun-Wen Kang [1]

1 Department of Chemical Engineering, Feng Chia University, 100, Wenhwa Road, Seatwen, Taichung 40724, Taiwan; wyj05@ms17.hinet.net (Y.-C.W.); ss0911445818@gmail.com (H.-C.Z.); wainss9407278@gmail.com (C.-W.K.)

2 Department of Chemical Engineering, i-Center for Advanced Science and Technology (ICAST), National Chung Hsing University, Eng Bld 3, 250 Kuo Kuang Road, Taichung 40227, Taiwan; HuangCF@dragon.nchu.edu.tw

* Correspondence: changcj@fcu.edu.tw

Abstract: The dual-functional Bi$_2$WO$_6$/polydopamine (PDA)-modified gauze membrane has been developed for applications in photocatalytic degradation and solar steam generation. Two types of membrane were prepared by changing the growth sequence of Bi$_2$WO$_6$ nanomaterials and PDA on gauze substrates. The spatial distribution of Bi$_2$WO$_6$ and polydopamine has a great influence on light absorption, photocatalytic degradation, and solar steam generation performances. Bi$_2$WO$_6$ photocatalysts can absorb short-wavelength light for the photocatalytic decoloration of organic dyes. The photothermal polydopamine can convert light into heat for water evaporation. Besides, the gauze substrate provides water transport channels to facilitate water evaporation. The morphology, surface chemistry, and optical properties of Bi$_2$WO$_6$-PDA modified gauzes were characterized by scanning electron microscopy, transmission electron microscopy, X-ray photoelectron spectroscopy, and diffuse reflectance spectra. The photothermal properties, wetting properties, and solar steam generation rates of the composite films were also studied. Degradation of 96% of indigo carmine was achieved after being irradiated for 120 min in the presence of G/PDA/BWN$_P$. The water evaporation rates of the G/BWP/PDA sample under the irradiation of an Xe lamp (light intensity = 1000 W/m^2) reached 1.94 kg·m^{-2}·h^{-1}.

Keywords: Bi$_2$WO$_6$; polydopamine; photocatalytic degradation; solar steam generation

1. Introduction

Developing practical approaches to obtain clean water and eliminate pollutants is an important issue for our society because of the increasing world population [1] and water contamination caused by various industrial production processes. Besides, since solar energy is a sustainable and renewable energy source, light energy has been widely utilized in photovoltaic [2,3], photothermal [4–6], and photocatalytic [7,8] applications. Solar energy-driven water production is significant for people living in remote areas without electricity supply [9]. Solar steam generation is a promising process to produce clean water from seawater [10,11] or contaminated water sources [12,13]. Meanwhile, photocatalysts can be applied to the photocatalytic degradation of organic pollutants or the reduction of heavy metal ions [14,15]. Pollutants can also be degraded in the presence of heat (thermocatalysis) or light (photocatalysis, photoactivation and photothermocatalysis) [16]. Therefore, the development of dual-functional membranes for water treatment by the combined solar steam generation and photocatalytic degradation approaches is worth studying. Yang et al. [17] developed a novel dual-functional water-treatment system by integrating photothermal Ti$_3$C$_2$T$_x$, La$_{0.5}$Sr$_{0.5}$CoO$_3$ photocatalysts, and polyvinyl alcohol/chitosan hydrogels. The system can achieve high photothermal conversion performance and photodegradation

activity. Jin et al. [18] reported that the $Pt/Au/TiO_2$ NP-wood carbon composite materials exhibited outstanding interfacial solar steam generation property and photocatalytic degradation activity toward tetracycline. Ding et al. [19] reported a large-scale outdoor solar conversion device that was constructed to simultaneously harvest freshwater from contaminated water and degrade organic dyes in the source water. The daily freshwater production rate is 5.7 kg m^{-2}. This demonstrated the potential of the membrane for the production of potable water and the treatment of contaminated water using one device.

The combination of polymer and inorganic materials was useful for improving various properties, such as solar steam generation, moisture blocking, photocatalytic degradation, photoconductive, and gas sensing [20–26] performance. Polydopamine (PDA) exhibits excellent adhesion, biocompatibility, hydrophilicity, and photothermal conversion properties [27]. It has been used for various applications, such as adsorbents for heavy metals ions [28,29], photothermal cancer therapy [30–32], and solar steam generation [33]. PDA was used in the preparation of some polymer/inorganic composite photocatalysts. PDA modification was effective in improving the activity of g-C3N4, BiOBr, BiOCl, ZnO, BiVO$_4$, and TiO$_2$-based composite photocatalysts that can be used for photocatalytic degradation, photocatalytic CO$_2$ reduction, and removal of hexavalent chromium [34–38]. Furthermore, polydopamine-inorganic composites were loaded on fabrics for catalysis applications. Liu et al. reported the preparation and properties of flexible Ag/AgCl/polydopamine/cotton fabric-based photocatalysts [39]. Wang and coworkers studied the UV protection, antimicrobial activity, and photocatalysis property of CuO/BiVO$_4$-polydopamine and ZnO/polydopamine-modified cotton fabrics [40,41].

In recent years, Bi-based photocatalysts have attracted lots of attention, due to their tunable morphology, unique electronic band structure, and excellent chemical stability [42–44]. Bismuth tungstate (Bi$_2$WO$_6$) photocatalyst was developed to remove organic pollutions due to its advantages, such as tunable morphology, excellent stability, low cost, and high photocatalytic activity [45,46]. The activity of photocatalysts can be improved by introducing conductive polymer, carbon nanotube, carbon dots, and metal substrate [47–50]. Since it is difficult for Bi$_2$WO$_6$ photocatalysts to be separated and collected for repeated operation, the growth of Bi$_2$WO$_6$ nanomaterial on a porous substrate to make the immobilized photocatalyst is worth developing. Bi$_2$WO$_6$ photocatalysts have been coated on different supporting materials such as indium-tin-oxide glass [51], stainless steel [52,53], and polyester fabric [54,55] to make immobilized photocatalysts, exhibiting some advantages such as enhanced photocatalytic activity, self-cleaning properties, and recyclability. Indigo is a widely used dye in the textile industry for the dyeing of blue jeans and other blue denim products [56]. Its strong intermolecular hydrogen bonding leads to a high melting point and poor solubility. Indigo carmine (IC) exhibits better solubility. However, it is carcinogenic and can cause severe health problems [57,58]. In this work, we studied the decolorization of an IC dye to evaluate the degradation by various photocatalysts. The utilization of gauze as the porous substrate to support the functional polydopamine and Bi$_2$WO$_6$ in this work has some advantages. Its interconnected pore structure can provide water transport channels for photothermal evaporation. Besides, it was reported that a rough surface could enhance light trapping of incident solar light by multi-scattering [59,60]. The large specific surface area of microporous gauze also increases the contact area between the loaded Bi$_2$WO$_6$ and pollutants in wastewater, leading to enhanced water treatment capacity.

Considering the high activity of Bi$_2$WO$_6$, together with the broad optical absorption and excellent photothermal conversion characteristics of PDA, two types of PDA-Bi$_2$WO$_6$-gauze-based dual-functional membranes, G/BWP/PDA and G/PDA/BWN$_P$, were developed by the sequential growth of Bi$_2$WO$_6$ nanomaterials and PDA on gauze substrates through microwave-assisted hydrothermal and self-polymerization methods. The effects of the spatial distribution of Bi$_2$WO$_6$ and polydopamine on the light absorption properties, photocatalytic degradation, and solar steam generation performances of these films were studied.

2. Experimental

2.1. Nomenclature

G, G/PDA, and G/PDA/BWNp mean the gauze substrate, gauze/polydopamine, and gauze/polydopamine/Bi$_2$WO$_6$ nanoparticles samples, respectively. G/BWP and G/BWP/PDA indicate the gauze/Bi$_2$WO$_6$ nanoplates and gauze/Bi$_2$WO$_6$ nanoplates/ polydopamine samples, respectively.

2.2. Preparation of Dual-Functional Membrane

The non-sterile non-woven rayon/polyester gauze is provided by YASCO Enterprise Corp. Two types of dual-functional film were developed by the sequential growth of Bi$_2$WO$_6$ nanomaterials and PDA on gauze substrates for applications in photocatalytic degradation and solar steam generation in this study.

For the first type of sample, polydopamine was grown on the gauze substrate by self-polymerization. A dopamine solution was prepared by dissolving 0.25 g of dopamine hydrochloride in 50 mL of deionized water. Then, a 2 M NaOH solution was used to tune the pH value of the solution to 8.5. The gauze substrate (2 cm × 2 cm) was immersed in the dopamine solution at room temperature for 24 h to make the G/PDA sample. Then, a uniform Bi$_2$WO$_6$ nanoparticle layer was formed by the alternative immersion of the G/PDA sample into separately placed Bi(NO$_3$)$_3$ (0.06 M, 50 mL) and Na$_2$WO$_4$ (0.06 M, 50 mL) solution for 3 min. Before immersion in another solution, the gauze-based sample was immersed in D.I. water for 1 min. The alternative immersion was repeated 10 times. Then, the G/PDA/BWNp sample was obtained after washing by water and drying at 60 °C for 24 h (Figure 1a).
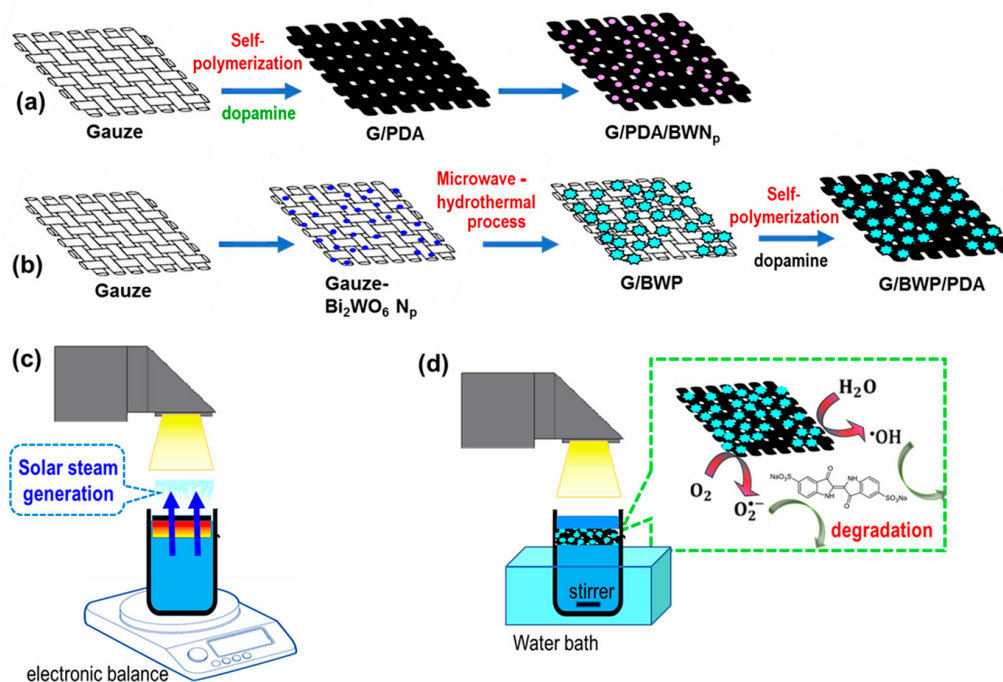

Figure 1. Procedures of the formation of Bi$_2$WO$_6$-polydopamine decorated gauze (**a**) G/PDA/BWNp (gauze/polydopamine/Bi$_2$WO$_6$ nanoparticles) (**b**) G/BWP/PDA (gauze/Bi$_2$WO$_6$ nanoplates/ poly-dopamine) samples, schematic illustrations of the setup for (**c**) solar steam generation test (**d**) photocatalytic degradation test.

For the second type of sample, G/BWP/PDA was prepared by the consecutive growth of Bi$_2$WO$_6$ nanomaterials and PDA on gauze substrates (Figure 1b). The Bi$_2$WO$_6$ nanomaterials were grown by a two-step process. At first, a uniform Bi$_2$WO$_6$ nanoparticle layer was formed on the gauze by the alternate immersion of the gauze substrate (2 cm × 2 cm)

into separately placed $Bi(NO_3)_3$ (0.06 M, 50 mL) and Na_2WO_4 (0.06 M, 50 mL) solution. Before the immersion in another solution, the gauze-based sample was rinsed with D.I. water for 1 min. The alternative immersion was repeated ten times. G/BWNp sample was obtained after washing by water and drying at 60 °C for 24 h. For the second step, Bi_2WO_6 nanoplates (BWP) were grown on the previous G/BWNp substrate to make the G/BWP sample by a microwave-assisted hydrothermal method. 0.365 g of $Bi(NO_3)_3$ was dissolved in 20 mL of ethylene glycol to prepare solution A. 0.125 g of Na_2WO_4 was dissolved in 20 mL of ethylene glycol to prepare solution B. The G/BWNp substrate (2 cm × 2 cm), solution A, and solution B were put in a EasyPrep Plus® closed vessels (100 mL). The reaction mixture was sealed and heated by a Microwave Synthesis System (MARS 6, CEM, NC, USA) at 160 °C for 20 min to make the G/BWP sample. Then, polydopamine was grown on the G/BWP by self-polymerization to make the G/BWP/PDA sample. A dopamine solution was prepared by dissolving 0.25 g of dopamine hydrochloride in 50 mL of deionized water. Then, a 2 M NaOH solution was used to tune the pH value of the solution to 8.5. The G/BWP sample (2 cm × 2 cm) was immersed in the prepared dopamine solution for 24 h at room temperature. Then, the G/BWP/PDA sample can be obtained after being washed with deionized water three times and dried at 60 °C (Figure 1b).

2.3. Solar Steam Generation

The solar steam generation test was performed to investigate the light-to-heat conversion performance of various samples (Figure 1c). A fluoro acrylate copolymer-based water repellent agent solution (JR7101, J-Young Technology Corp., Hsinchu city, Taiwan) was spray-coated on the top layer of the sample (2 cm × 2 cm) and dried at 60 °C for 10 min to make the sample floatable. In the solar steam generation experiment, 20 mL of water was added to a beaker with a diameter of 2.9 cm (height 4.1 cm), and the sample was floated on the water. The light intensity of the simulated solar light (Xenon lamp, PX350A, Prosper OptoElectronic Co., New Taipei City, Taiwan) was tuned at 1000 W/m^2. The thermal images and surface temperature of the membranes floating on the solution were monitored by an infrared thermal imaging camera (FLIR-A320, FLIR SYSTEMS, Wilsonville, OR, USA). An analytical balance (GF2000, A&D, Tokyo, Japan) connected to a computer was used for real-time monitoring of the mass changes during the photothermal evaporation test. The whole evaporation process was carried out under the ambient temperature of 30 °C and relative humidity of 70%.

2.4. Photocatalytic Degradation

The photocatalytic activities were evaluated for the decoloration of the indigo carmine solution under light irradiation. The photocatalytic degradation of indigo carmine dye was performed in a reactor using 10 mL of a 60 ppm dye solution and the photocatalysts (2 cm × 2 cm). Before the irradiation, the solution was magnetically stirred for 60 min in the dark to reach an absorption-desorption equilibrium. These solutions were illuminated with a 350 W Xe lamp (Prosper HID). The temperature of the solution was maintained at 30 °C using a water bath. The dye degradation was monitored by a JASCO V-770 UV-vis spectrophotometer.

2.5. Characterization

The morphologies of samples were analyzed with a field scanning electron microscope (FESEM, HITACHI, S-4800) and a field-emission transmission electron microscope (TEM, JEOL, JEM-2100F). The surface chemical composition and elemental valence were identified from X-ray photoelectron spectra (XPS, ULVAC-PHI, PHI 5000 Versa Probe), using C 1s peak as a reference to calibrate binding energies. The surface wettability of the samples was evaluated with a contact-angle meter (CAM-100, Creating-Nanotech Co., Tainan city, Taiwan). The Raman spectrum was measured by a Raman microscope (MRI532S, Protrustech, Tainan city, Taiwan) with an emission wavelength of 532 nm (He–Ne laser). The detector integration time and laser irradiation power were 10 s and 2 mW. The diffuse reflectance

spectra (DRS) were recorded by a spectrometer (JASCO V-770, Tokyo, Japan) to measure the light absorption property of photocatalysts.

3. Results and Discussion

3.1. Morphology

The fiber surface morphology of the membrane changed after the growth of Bi_2WO_6 nanoplates and polydopamine on the surface of gauze, as observed by the FESEM images. Figure 2 illustrates the FESEM images of gauze, G/PDA, G/PDA/BWNp, G/BWP, and G/BWP/PDA samples. As shown in Figure 2a,f, the fibers of pristine gauze show a smooth surface with a diameter ranging between 9 to 11 μm. The polydopamine was grown on the gauze substrate by self-polymerization to enable the G/PDA sample to act as a comparative sample. Parts of the surfaces of PDA-modified fibers for G/PDA are covered by some particles with the size ranging from 150 nm to 500 nm, due to the polymerization of dopamine (Figure 2b,g). Then, Bi_2WO_6 nanoparticles (BWNp) were grown on the surface of G/PDA by a successive ionic layer adsorption and reaction process to prepare G/PDA/BWNp sample. As shown in Figure 2c,h, BWNp with the size of less than 100 nm was uniformly distributed on almost all the fiber surfaces of G/PDA/BWNp. The Bi_2WO_6 nanomaterials were grown by a two-step process to achieve uniform modification of the fiber surface. The first step was a successive ionic layer adsorption and reaction route. The second step was a microwave-assisted hydrothermal process. The morphology of the G/BWP sample (Bi_2WO_6 nanoplate modified gauze) is shown in Figure 2d,i. For the G/BWP sample, the surface of the fiber is fully covered with a lot of assembled two-dimensional Bi_2WO_6 nanoplates. The enlarged image of the G/BWP sample (Figure 2i) shows that Bi_2WO_6 grows into two-dimension rectangular-plate-like morphologies with a side length of 5–10 μm and the width of 1.0–5.5 μm. The thickness of an individual Bi_2WO_6 nanoplate is 0.22–1.1 μm. Bi_2WO_6 nanoplates were randomly stacked together. Besides, the fiber diameter of G/BWP increases, ranging between 35 to 55 μm (Figure 2d). The increased fiber diameter results from the formation of large amounts of nanoplates on the fiber surface. Then, polydopamine was grown on the surface of G/BWP to make the G/BWP/PDA sample. Figure 2e,j show that randomly stacked Bi_2WO_6 nanoplates were still observed on G/BWP/PDA. Besides, compared to the enlarged image of G/BWP (Figure 2i), there are lots of PDA nanoparticles formed on the Bi_2WO_6 nanoplates (Figure 2j). The fiber diameter of G/BWP/PDA (Figure 2d) is close to G/BWP (Figure 2e).
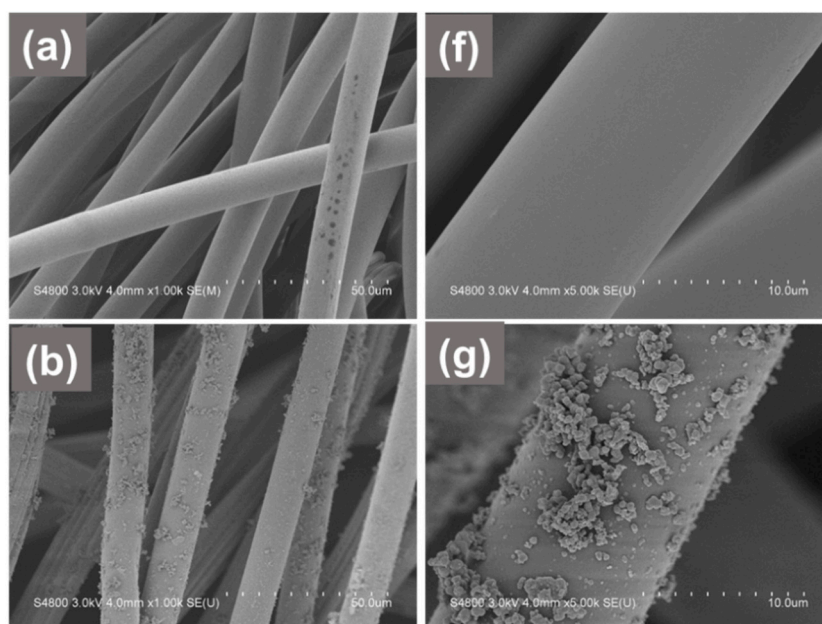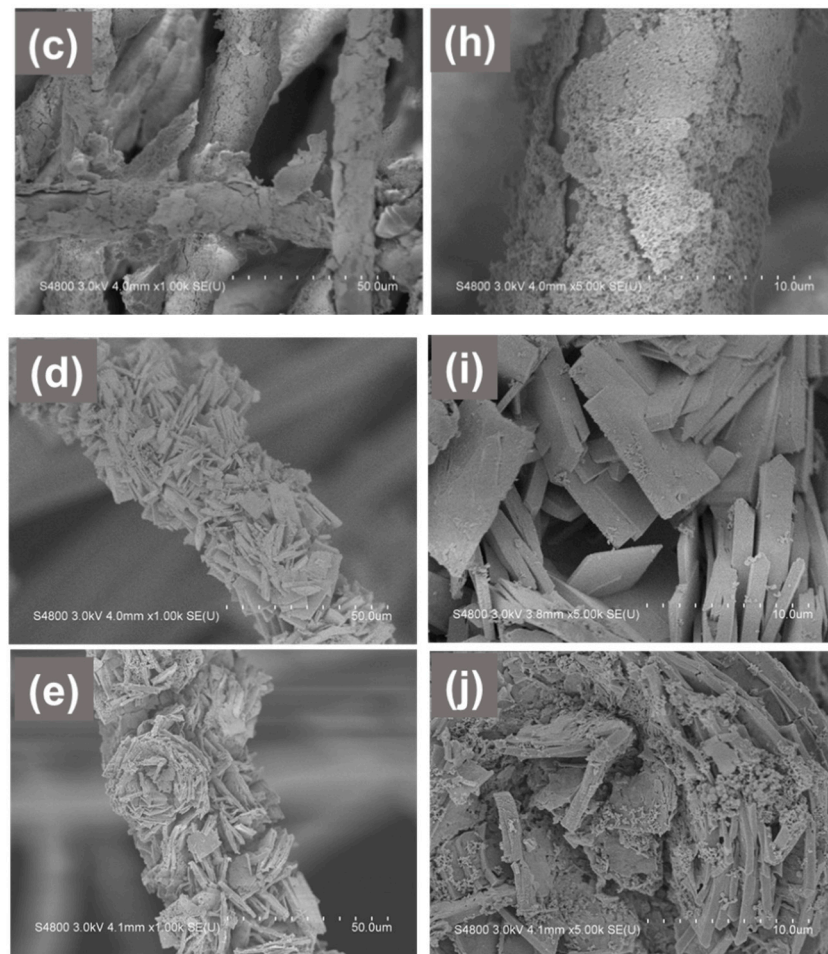

Figure 2. *Cont.*

Figure 2. Field-emission scanning electron microscopy (FESEM) images of (**a**,**f**) gauze (**b**,**g**) G/PDA (**c**,**h**) G/PDA/BWNp (**d**,**i**) G/BWP (**e**,**j**) G/BWP/PDA.

3.2. Chemical Compositions

3.2.1. Transmission Electron Microscopy Energy-Dispersive X-ray (TEM EDX)

The TEM energy-dispersive X-ray (EDX) spectrum of a line scan is presented in Figure 3a to investigate the elemental distribution for the powder scratched from the G/BWP/PDA composite sample. The Bi, W, O, and N elements are found in the G/BWP/PDA sample. The elements of Bi, W, and O indicate the existence of Bi_2WO_6. The N element originates from dopamine due to the successful polymerization of dopamine on the fabrics. The signals of the Bi, W, O, and N elements are higher near the center of the line, indicating that the plate-like sample is Bi_2WO_6, and polydopamine is distributed well near Bi_2WO_6. Similar results were observed for the powder scratched from the G/PDA/BWNp composite sample (Figure 3b).

3.2.2. X-ray Photoelectron Spectra (XPS) Analysis

The XPS analysis of G/BWP/PDA sample was measured to analyze its oxidation state and chemical composition. Figure 4 shows the XPS (a) Bi 4f (b) W 4f (c) N 1s (d) O 1s spectra of G/BWP/PDA. The Bi 4f peaks of G/BWP/PDA at 158.9 and 164.2 eV can be assigned to Bi $4f_{7/2}$ and Bi $4f_{5/2}$, indicating the Bi^{3+} of Bi_2WO_6. The W 4f peaks of G/BWP/PDA at 37.8 and 34.7 eV are attributed to W $4f_{5/2}$ and W $4f_{7/2}$, respectively, which are related to W^{6+} of Bi_2WO_6 [61,62]. The N 1s peak is deconvoluted into three peaks (Figure 4c). That peaks at 401.5, 399.8, and 398.7 eV can be attributed to primary amine (R–NH_2), secondary amine (R1-NH-R2), and tertiary amine (=N-R) groups, respectively [63,64]. The results are related to the chemical structures of polydopamine, possible intermediate species,

and dopamine monomer [65]. The primary amine is related to dopamine. The secondary amine can be assigned to the intermediate species or polydopamine, while the tertiary amine can be attributed to tautomeric species of the intermediates. The O 1s spectrum of G/BWP/PDA was deconvoluted into two peaks. The peaks at 531.3 and 532.7 eV are assigned to Bi–O, and O–H, respectively. These results support the formation of Bi_2WO_6 and polydopamine on the sample. Figure 4e–h present the XPS Bi 4f, W 4f, N 1s, and O 1s spectra of G/PDA/BWNp, respectively. The results of the G/PDA/BWNp sample were similar to those of G/BWP/PDA, except that the Bi–O peak was higher than the O–H peak in the O 1s spectrum.
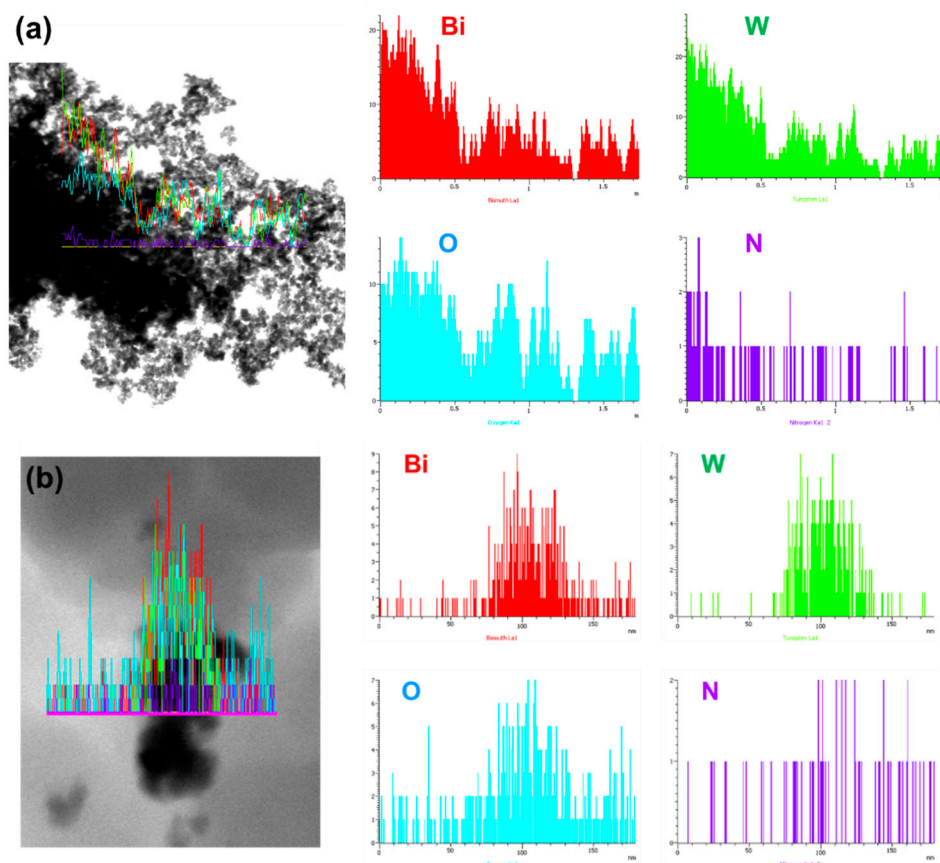

Figure 3. Transmission electron microscopy (TEM) image and energy-dispersive X-ray (EDX) spectrum of line scan of (**a**) G/BWP/PDA (**b**) G/PDA/BWNp.

3.2.3. Raman Spectra

The surface chemistry of G/BWP/PDA and G/PDA/BWN$_P$ was analyzed by the Raman spectra (Figure 5). The peak at 709 cm^{-1} is associated with the asymmetric stretching mode of WO_6 octahedra for the vibrations of equatorial oxygen atoms within layers. The peak at 307 cm^{-1} was related to the simultaneous translational movement of Bi^{3+} and the bending of WO_6 octahedra [66,67]. Besides, two broad peaks at 1343 and 1584 cm^{-1} were attributed to the catechol stretching vibration and deformation from the chains of polydopamine. Similar results were reported in the literature [68–71]. These peaks support the existence of polydopamine and Bi_2WO_6 on G/BWP/PDA sample. Similar peaks were found for the G/PDA/BWN$_P$ sample.
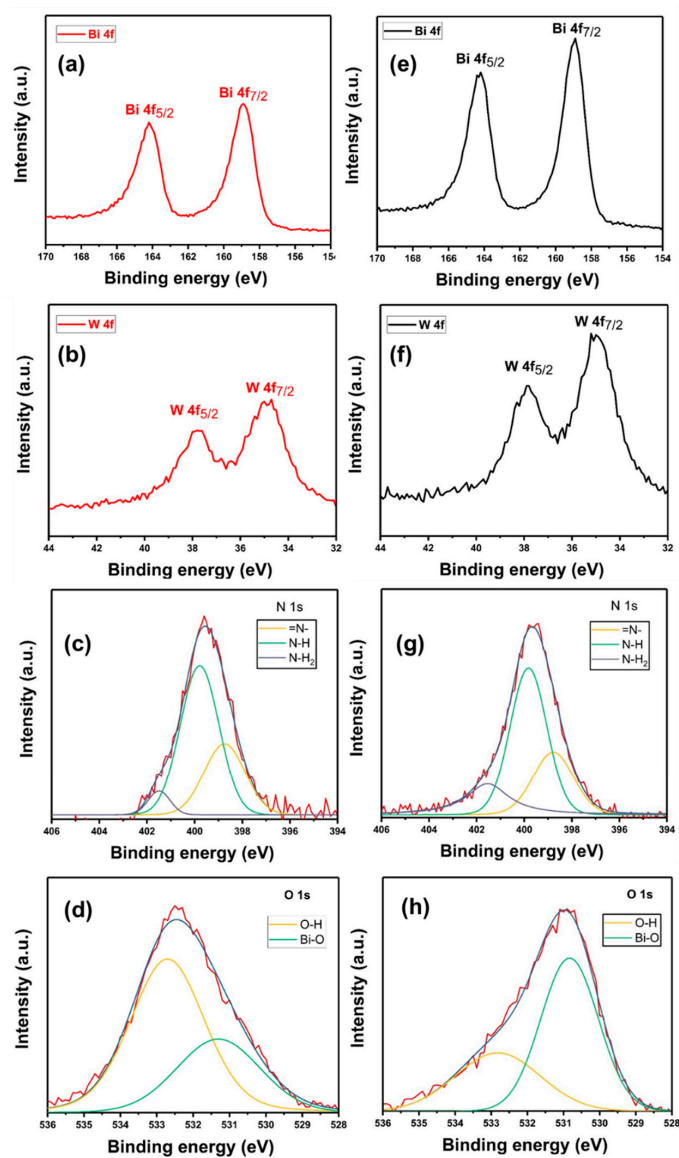
Figure 4. X-ray photoelectron spectra (XPS) (**a**) Bi 4f (**b**) W 4f (**c**) N 1s (**d**) O 1s of G/BWP/PDA and XPS (**e**) Bi 4f (**f**) W 4f (**g**) N 1s (**h**) O 1s spectra of G/PDA/BWNp.
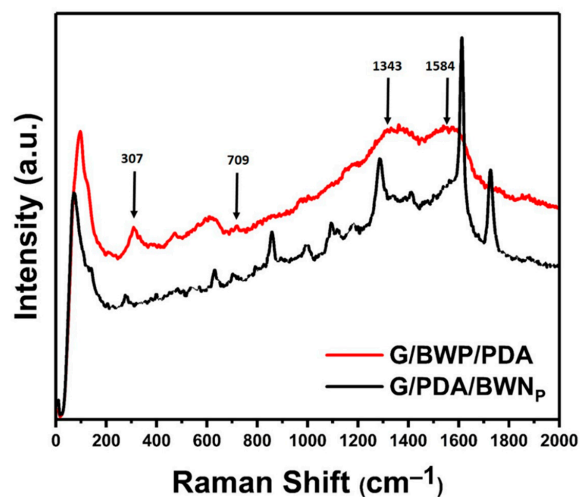

Figure 5. Raman spectra of G/BWP/PDA and G/PDA/BWN$_P$.

3.3. Diffuse Reflection Spectra (DRS)

The light absorption properties of various samples were observed by a diffuse reflection spectrophotometer. G/BWP samples (Figure 6a) showed a strong light absorption in the UV region ranging from 200 to 380 nm. Compared with the G/BWP samples, G/BWP/PDA exhibits an increase in UV and visible light absorption ranging from 200 to 800 nm. The G/PDA membrane exhibits the highest UV and visible light absorption among the four samples. After the decoration of BWN_P on the G/PDA, the $G/PDA/BWN_P$ sample showed decreased light absorption than the G/PDA membrane. The results of G/BWP/PDA and $G/PDA/BWN_P$ exhibit the influences of the spatial distribution of Bi_2WO_6 and polydopamine on the light absorption properties of G/BWP/PDA and $G/PDA/BWN_P$. The composition that appeared on the top layer exhibits a greater influence on the light absorption of the composite membrane. G/BWP/PDA with polydopamine on the top layer show larger absorption in the visible light region, while the $G/PDA/BWN_P$ sample has higher absorption in the UV light range. Figure 6b presents the Tauc plots of G/BWP, G/BWP/PDA, G/PDA, and $G/PDA/BWN_P$. The bandgaps of two types of Bi_2WO_6 (BWP and BWN_p) were obtained from G/BWP and $G/PDA/BWN_P$ samples because the Bi_2WO_6 nanomaterials were located on their top layer. The bandgaps of BWP and BWN_p were 3.33 and 3.35 eV, respectively.
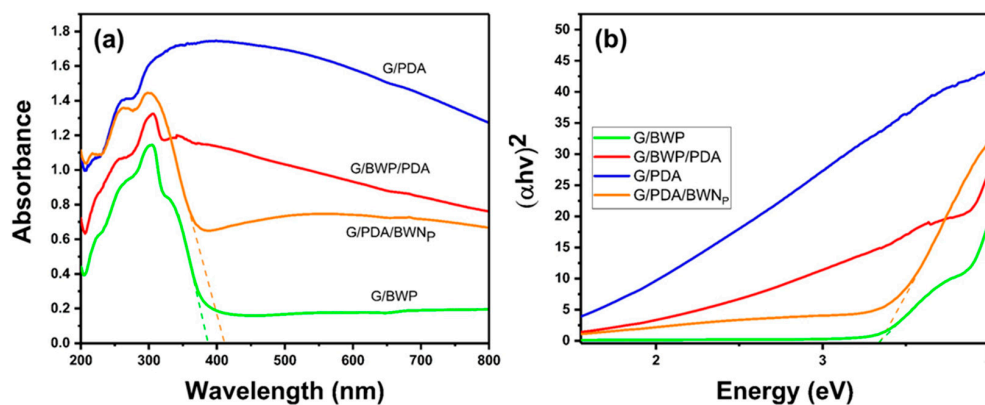

Figure 6. (**a**) Diffuse reflection spectra (DRS) (**b**) Tauc plot of G/BWP, G/BWP/PDA, G/PDA, and $G/PDA/BWN_P$.

3.4. X-ray Diffraction (XRD) Spectra

Figure 7 presents the XRD spectra of $G/PDA/BWN_P$ and G/BWP/PDA. A broad diffraction peak of $G/PDA/BWN_P$ photocatalyst at $2\theta = 28.4°$ is assigned to the (131) plane of the orthorhombic phase of Bi_2WO_6 (JCPDS#79-2381). There is a wide peak at around $2\theta = 50°$. The broad XRD diffraction peaks indicated weak crystallinity of the $G/PDA/BWN_P$ photocatalyst. The main characteristic diffraction peaks of the G/BWP/PDA photocatalyst observed at $2\theta = 28.4°$, $32.8°$, $47.2°$, and $55.7°$ are attributed to the (131), (200), (202), and (133) planes of the orthorhombic phase of Bi_2WO_6 (JCPDS#79-2381), respectively. These were consistent with the results reported in other literature [72,73], indicating the formation of Bi_2WO_6 in G/BWP/PDA.

3.5. Surface Hydrophilicity

An efficient water supply is essential to the preparation of an effective solar steam generation membrane. In this study, the SEM images of modified samples revealed that the porous structures of gauze substrates remained after the growth of polydopamine and Bi_2WO_6 nanomaterials. These encapsulated materials should be hydrophilic to facilitate water supply and steam escape. The surface hydrophilicity also facilitates the contact between the photocatalyst and the organic pollutant. The surface hydrophilicity was evaluated by measuring the dynamic contact angles of water droplets on different samples (without coating the hydrophobic layer) to elucidate their potential applications in solar

evaporation and photocatalytic degradation. As shown in Figure 8a, the complete wetting of a water droplet on pristine gauze was achieved within 6.83 s. However, G/PDA (Figure 8b), G/BWP (Figure 8c), G/BWP/PDA (Figure 8d), and G/PDA/BWN$_P$ (Figure 8e) samples exhibited rapid, complete wetting within 0.033 s. The surface hydrophilicity was further enhanced after the loading of polydopamine and Bi$_2$WO$_6$ nanomaterials.
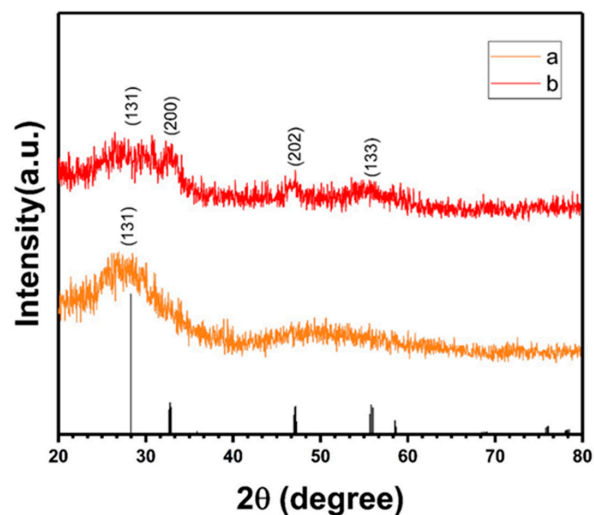

Figure 7. X-ray diffraction (XRD) spectra of (**a**) G/PDA/BWN$_P$ (**b**) G/BWP/PDA.
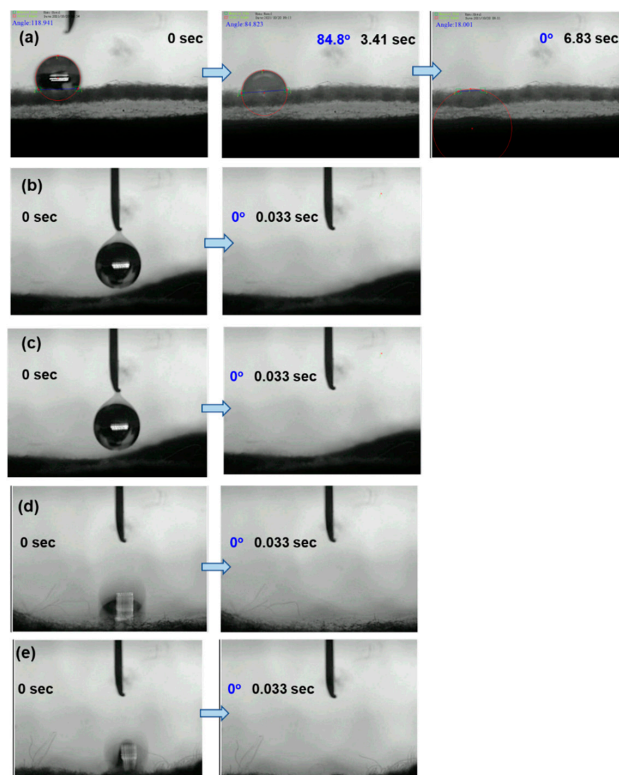
Figure 8. Dynamic contact angles of water droplets on (**a**) gauze (**b**) G/PDA (**c**) G/BWP (**d**) G/BWP/PDA (**e**) G/PDA/BWN$_P$.

3.6. Photocatalytic Property

The activity of different immobilized photocatalysts (G/BWN$_P$, G/BWP, G/BWP/PDA) under light illumination was investigated through photocatalytic decoloration experiments using indigo carmine (IC) as the pollutant model compound. The photocatalytic degra-

dation performance of various samples is shown in Figure 8. The initial concentration of indigo carmine (60 ppm) and the size of the membrane (2 cm × 2 cm) were kept the same in all experiments for the comparison of different samples. For the Bi_2WO_6 nanoplates-based G/BWP sample, 39% of IC was adsorbed on the photocatalyst during the dark test (Figure 9a). The absorption peak of residual IC solution at 610 nm decreases rapidly under light irradiation, indicating the high photocatalytic degradation activity of G/BWP. 99% of IC can be degraded after the irradiation for 60 min in the presence of G/BWP. However, the IC adsorption property changed when PDA was grown on G/BWP. No noticeable decrease of IC was observed for the dark test of the G/BWP/PDA sample, indicating the adsorption of IC on the G/BWP/PDA was negligible (Figure 9b). Besides, the photocatalytic degradation activity of G/BWP/PDA was lower than that of G/BWP. The residual concentration of IC solution decreases gradually after light irradiation. The irradiation time required for degradation of 99% IC by G/BWP/PDA is 210 min. Such a decrease in the photocatalytic activity of the G/BWP/PDA sample may result from the coverage of B_2WO_6 nanoplates by polydopamine, leading to a reduction in the exposed active sites of B_2WO_6 nanoplates. Such a problem can be solved by changing the formation sequence of Bi_2WO_6 and polydopamine on the gauze substrate. The G/PDA/BWN$_P$ photocatalyst was prepared by the deposition of polydopamine on the gauze substrate by self-polymerization, followed by the formation of a uniform Bi_2WO_6 nanoparticle layer on top. Compared with G/BWP/PDA, the photocatalytic activity of the G/PDA/BWN$_P$ membrane was improved. Degradation of 96% of IC was achieved after being irradiated for 120 min in the presence of G/PDA/BWN$_P$ (Figure 8c). Photodegradation of indigo carmine (60 ppm) without photocatalyst was shown in Figure 9d as a blank test. Its decoloration rate was slower than other three curves with different photocatalysts. De Andrade et al. [74] studied the degradation of the indigo carmine dye in aqueous medium by the autoclaved cellular concrete/Fe_2O_3 catalyst in Fenton-like and photocatalytic processes. The toxicity tests against Vero cells indicated that the toxicity of the degradation products, generated by both processes, is smaller or similar to the precursor dye. Vautier et al. [56] reported the photocatalytic degradation of indigo carmine using UV-irradiated titania-based catalysts. The oxidative agents are photo-produced holes h^+ and/or •OH radicals. A detailed degradation pathway, based on careful identification of intermediate products, is proposed. In addition to a prompt removal of the color, photocatalysis can mineralize carbon and of nitrogen and sulfur heteroatoms into innocuous compounds. In our previous study [53], the photocatalytic degradation by Ag/flower-like Bi_2WO_6 photocatalysts with and without scavengers reveals that h^+ and •O_2^- are the major active species generated by the photocatalyst. The oxidation of water by holes can generate •OH. We believe the products of the photocatalytic degradation using Bi_2WO_6 photocatalysts will not be more toxic than the parent compound, indigo carmine.

3.7. Solar-Steam Generation

The photothermal and solar steam generation performance of various samples (G/PDA, G/BWP/PDA, gauze) were evaluated. Typical infrared thermal images and the surface temperature changes of different membranes recorded by an infrared camera are shown in Figure 10a,b, respectively. Figure 10a reveals that the temperatures around the floated composite films are all higher than the bulk solution. Figure 10b shows the surface temperature profiles of G/PDA, G/BWP/PDA, G/PDA/BWN$_P$, and gauze samples versus time under the simulated solar illumination. Before the light illumination, the initial surface temperature of all samples is about 30 °C. After the simulated solar illumination with a power density of 1000 W m^{-2} for 1 h, the surface temperature of the gauze is 36.1 °C. However, the surface temperatures of G/PDA and G/BWP/PDA samples reached 67.4 and 65.7 °C, respectively. These two samples with PDA on the top layer showed similar surface temperatures. The Bi_2WO_6 nanoplates under the PDA polymer did not deteriorate the light-to-heat transform property of polydopamine. Han et al. [75] studied the dual functional polydopamine-modified CuS@HKUST for quick sterilization through enhanced photother-

mal and photocatalytic ability. They found that the nanoparticles' ability to produce heat was improved after the coating of polydopamine. Compared with G/BWP/PDA, the G/PDA membrane exhibits higher light absorption (Figure 6) and photothermal-induced temperature rise (Figure 10a). The surface temperature of G/PDA/BWN$_P$ (49.0 °C) is lower than that of G/PDA. The Bi$_2$WO$_6$ nanomaterials exhibit lower light absorption than PDA (Figure 6). PDA also has excellent photothermal conversion properties. It may explain why the coverage of polydopamine by B$_2$WO$_6$ nanoparticles leads to the decrease of surface temperature from 67.4 (G/PDA) to 49.0 °C (G/PDA/BWN$_P$). The distribution of PDA and Bi$_2$WO$_6$ on the samples has some influences on the temperature increase. G/BWP/PDA with PDA-coated G/BWP structure exhibit a higher temperature increase than the G/PDA/BWN$_P$ sample with BWN$_P$-coated G/PDA structure. The surface temperatures reached the maximum values for all samples after 10 min of irradiation (Figure 10b). The photothermal-induced temperature rise of gauze (as a comparative sample) was much lower than G/PDA and G/BWP/PDA. The results indicate the high light absorption and effective photothermal conversion properties of these PDA-based samples (G/PDA, G/BWP/PDA, G/PDA/BWN$_P$). Meanwhile, polydopamine is the critical component for the photothermal conversion properties of composite materials. Figure 10c presents the mass loss of water over time by G/PDA, G/BWP/PDA, gauze after simulated solar illumination at 1 kW m^{-2}. The water evaporation rates of the Bi$_2$WO$_6$-PDA based films did not follow the trend of the light-induced temperature rise. The water evaporation rates of the G/BWP/PDA sample under the irradiation of the Xe lamp (light intensity = 1000 W/m^2) reached 1.94 kg·m^{-2}·h^{-1}. Although the G/PDA and G/BWP/PDA films exhibited similar light-induced temperature rise, G/BWP/PDA showed a higher water evaporation rate than the G/PDA film (1.68 kg·m^{-2}·h^{-1}). The water evaporation rates of the functional films depend on the photothermal effect of the material, film structure for water supply and steam escape, and thermal management [76]. As shown in the SEM images (Figure 2), there are interstices among the Bi$_2$WO$_6$ nanoplates for G/BWP/PDA. Compared with the G/PDA film, the G/BWP/PDA sample with Bi$_2$WO$_6$ nanoplate aggregates on the fiber surface may provide a better capillary structure for water supply and steam escape. Besides, both the G/PDA and G/BWP/PDA films showed higher water evaporation rates than the gauze (0.93 kg m^{-2} h^{-1}). The G/PDA/BWN$_P$ membrane shows a higher water evaporation rate (1.83 kg m^{-2} h^{-1}) than the G/PDA sample (Figure 10c). The Bi$_2$WO$_6$ nanomaterials may contribute to water transport and steam escape. These photothermal membranes can convert light energy into localized heat and vaporize water across the microporous surface into steam.
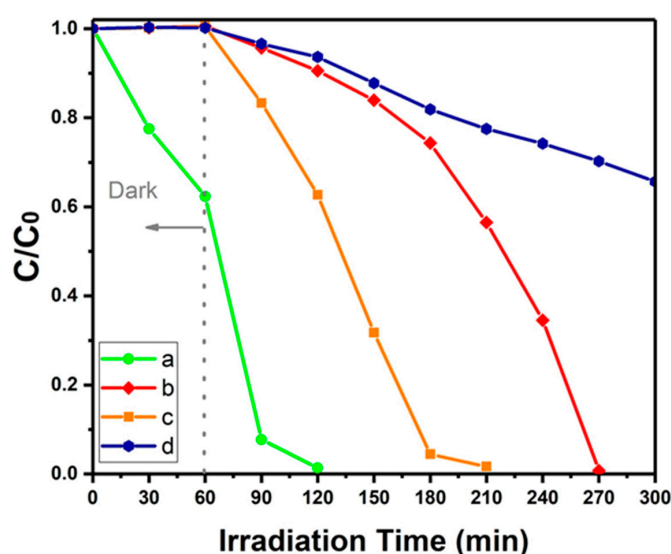

Figure 9. Photodegradation of indigo carmine (60 ppm) under circulating water conditions by (**a**) G/BWP (**b**) G/BWP/PDA (**c**) G/PDA/BWN$_P$ (**d**) without photocatalyst (blank).
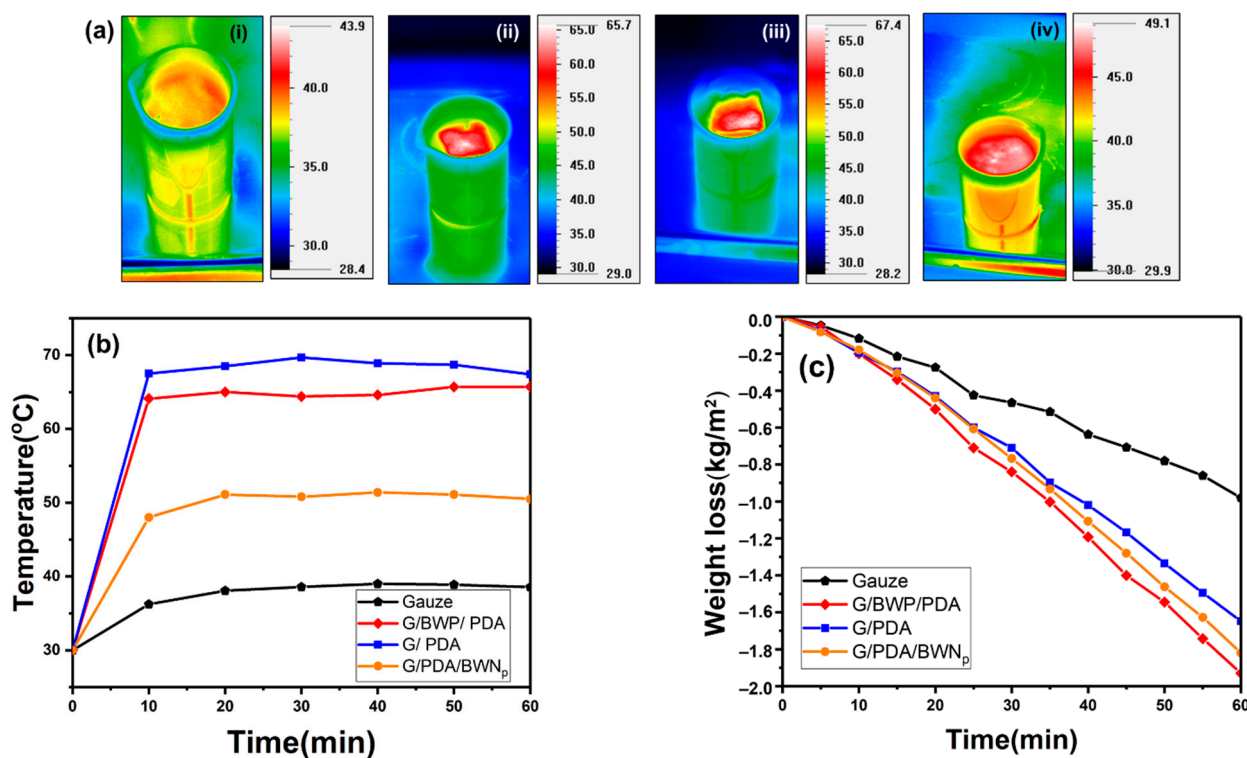
Figure 10. (**a**) Bulk water temperature distribution of (i) gauze (ii) G/BWP/PDA (iii) G/PDA (iv) G/PDA/BWN$_P$, and (**b**) surface temperature profiles over time (**c**) mass loss of water over time by gauze, G/PDA, G/BWP/PDA, G/PDA/BWN$_P$ after simulated solar illumination at 1 kW m^{-2} (1 sun).

4. Conclusions

A Bi$_2$WO$_6$-polydopamine (PDA) modified gauze was developed as a dual-functional membrane for application in photocatalytic degradation and solar steam generation. The spatial distribution of Bi$_2$WO$_6$ and polydopamine has a great influence on the light absorption properties, photocatalytic degradation, and solar steam generation performances of G/BWP/PDA and G/PDA/BWN$_P$. G/BWP/PDA with polydopamine on the top layer showing a higher photothermal temperature rise. G/PDA/BWN$_P$ with Bi$_2$WO$_6$ nanoparticles on top exhibit higher photocatalytic activity and similar solar steam generation performance when compared with G/BWP/PDA. Active sites of Bi$_2$WO$_6$ nanoparticles that were not covered by polydopamine may contribute to the improved photocatalytic performance of G/PDA/BWN$_P$. For the G/BWP/PDA and G/PDA/BWN$_P$ with better solar steam generation performance than G/PDA, the Bi$_2$WO$_6$ nanomaterials may contribute to the water transport and steam escape. The membrane with an interconnected pore structure can facilitate the contact between Bi$_2$WO$_6$ and dye pollutants, and the capillary transport of water to the top surface. Degradation of 96% of IC was achieved after irradiation for 120 min in the presence of G/PDA/BWN$_P$. The photothermal water evaporation rate and surface temperature of the G/BWP/PDA membrane under irradiation (1 sun) reached 1.94 kg m^{-2} h^{-1} and 65.7 °C, respectively. For the application of water production in remote areas without electricity supply, a dual-functional membrane (G/BWP/PDA or G/PDA/BWPNp) using a ternary compound may be a good choice. People can collect clean water by condensing the solar-generated water vapor, and can degrade the pollutant before it flows into the water body.

Author Contributions: C.-J.C., Y.-C.W. and C.-F.H. conceived the ideas and designed the experiments; Y.-C.W., H.-C.Z. and C.-W.K. performed the experiments; Y.-C.W. and C.-J.C. analyzed the data and wrote the paper. All authors have read and agreed to the published version of the manuscript.

Institutional Review Board Statement: Not applicable.

Informed Consent Statement: Not applicable.

Data Availability Statement: The data presented in this study are available on request from the corresponding author.

Conflicts of Interest: The authors declare no conflict of interest.

References

1. Liu, X.; Wang, X.; Huang, J.; Cheng, G.; He, Y. Volumetric solar steam generation enhanced by reduced graphene oxide nanofluid. *Appl. Energy* **2018**, *220*, 302–312. [CrossRef]
2. Ha, J.W.; Park, J.B.; Park, H.J.; Hwang, D.H. Novel Conjugated Polymers Containing 3-(2-Octyldodecyl) thieno [3, 2-b] thiophene as a π-Bridge for Organic Photovoltaic Applications. *Polymers* **2020**, *12*, 2121. [CrossRef]
3. Barretta, C.; Oreski, G.; Feldbacher, S.; Resch-Fauster, K.; Pantani, R. Comparison of Degradation Behavior of Newly Developed Encapsulation Materials for Photovoltaic Applications under Different Artificial Ageing Tests. *Polymers* **2021**, *13*, 271. [CrossRef] [PubMed]
4. Wang, C.F.; Wu, C.L.; Kuo, S.W.; Hung, W.S.; Lee, K.J.; Tsai, H.C.; Chang, C.J.; Lai, J.Y. Preparation of Efficient Photothermal Materials from Waste Coffee Grounds for Solar Desalination and Water Purification. *Sci. Rep.* **2020**, *10*, 1–10.
5. Hu, N.; Xu, Y.; Liu, Z.; Liu, M.; Shao, X.; Wang, J. Double-layer cellulose hydrogel solar steam generation for high-efficiency desalination. *Carbohydr. Polym.* **2020**, *243*, 116480. [CrossRef]
6. Mohsenpour, M.; Motahari, S.; Tajabadi, F.; Najafi, M. Preparation and application of sunlight absorbing ultra-black carbon aerogel/graphene oxide membrane for solar steam generation systems. *RSC Adv.* **2020**, *10*, 41780–41790. [CrossRef]
7. Chang, C.J.; Lee, Z.; Chu, K.W.; Wei, Y.H. CoFe$_2$O$_4$@ZnS core–shell spheres as magnetically recyclable photocatalysts for hydrogen production. *J. Taiwan Inst. Chem. Eng.* **2016**, *66*, 386–393. [CrossRef]
8. Senasu, T.; Nijpanich, S.; Juabrum, S.; Chanlek, N.; Nanan, S. CdS/BiOBr heterojunction photocatalyst with high performance for solar-light-driven degradation of ciprofloxacin and norfloxacin antibiotics. *Appl. Surf. Sci.* **2021**, *567*, 150850. [CrossRef]
9. Xu, Y.; Liu, D.; Xiang, H.; Ren, S.; Zhu, Z.; Liu, D.; Xu, H.; Cui, F.; Wang, W. Easily scaled-up photo-thermal membrane with structure-dependent auto-cleaning feature for high-efficient solar desalination. *J. Membr. Sci.* **2019**, *586*, 222–230. [CrossRef]
10. Wilson, H.M.; Ahirrao, D.J.; Ar, S.R.; Jha, N. Biomass-derived porous carbon for excellent low intensity solar steam generation and seawater desalination. *Sol. Energy Mater. Sol. Cells* **2020**, *215*, 110604. [CrossRef]
11. Wilson, H.M.; Ar, S.R.; Jha, N. Plant-derived carbon nanospheres for high efficiency solar-driven steam generation and seawater desalination at low solar intensities. *Sol. Energy Mater. Sol. Cells* **2020**, *210*, 110489. [CrossRef]
12. Higgins, M.W.; Rahmaan, A.S.; Devarapalli, R.R.; Shelke, M.V.; Jha, N. Carbon fabric based solar steam generation for waste water treatment. *Sol. Energy* **2018**, *159*, 800–810. [CrossRef]
13. Ibrahim, I.; Seo, D.H.; McDonagh, A.M.; Shon, H.K.; Tijing, L. Semiconductor photothermal materials enabling efficient solar steam generation toward desalination and wastewater treatment. *Desalination* **2021**, *500*, 114853. [CrossRef]
14. Abinaya, M.; Govindan, K.; Kalpana, M.; Saravanakumar, K.; Prabavathi, S.L.; Muthuraj, V.; Jang, A. Reduction of hexavalent chromium and degradation of tetracycline using a novel indium-doped Mn$_2$O$_3$ nanorod photocatalyst. *J. Hazard. Mater.* **2020**, *397*, 122885. [CrossRef] [PubMed]
15. Chang, C.J.; Chao, P.Y.; Lin, K.S. Flower-like BiOBr decorated stainless steel wire-mesh as immobilized photocatalysts for photocatalytic degradation applications. *Appl. Surf. Sci.* **2019**, *494*, 492–500. [CrossRef]
16. Bellardita, M.; Fiorenza, R.; D'Urso, L.; Spitaleri, L.; Gulino, A.; Compagnini, G.; Compagnini, G.; Scirè, S.; Palmisano, L. Exploring the photothermo-catalytic performance of Brookite TiO$_2$-CeO$_2$ composites. *Catalysts* **2020**, *10*, 765. [CrossRef]
17. Fan, D.; Lu, Y.; Zhang, H.; Xu, H.; Lu, C.; Tang, Y.; Yang, X. Synergy of photocatalysis and photothermal effect in integrated 0D perovskite oxide/2D MXene heterostructures for simultaneous water purification and solar steam generation. *Appl. Catal. B* **2021**, *295*, 120285. [CrossRef]
18. Wang, M.; Wang, P.; Zhang, J.; Li, C.; Jin, Y. A Ternary Pt/Au/TiO$_2$-Decorated Plasmonic Wood Carbon for High-Efficiency Interfacial Solar Steam Generation and Photodegradation of Tetracycline. *ChemSusChem* **2019**, *12*, 467–472. [CrossRef]
19. Ding, Y.; Feng, K.; He, P.; Liu, N.; Hao, L.; Gong, J.; Niu, R.; Qu, J. A synergistic photothermal and photocatalytic membrane for efficient solar-driven contaminated water treatment. *Sustain. Energy Fuels* **2021**, *5*, 5627–5637. [CrossRef]
20. Shao, B.; Wang, Y.; Wu, X.; Lu, Y.; Yang, X.; Chen, G.Y.; Owens, G.; Xu, H. Stackable nickel–cobalt@ polydopamine nanosheet based photothermal sponges for highly efficient solar steam generation. *J. Mater. Chem. A* **2020**, *8*, 11665–11673. [CrossRef]
21. Tsai, M.H.; Chang, C.J.; Lu, H.H.; Liao, Y.F.; Tseng, I.H. Properties of magnetron-sputtered moisture barrier layer on transparent polyimide/graphene nanocomposite film. *Thin Solid Film.* **2013**, *544*, 324–330. [CrossRef]
22. Nosrati, R.; Olad, A.; Maramifar, R. Degradation of ampicillin antibiotic in aqueous solution by ZnO/polyaniline nanocomposite as photocatalyst under sunlight irradiation. *Environ. Sci. Pollut. Res.* **2012**, *19*, 2291–2299. [CrossRef] [PubMed]

23. Wu, Y.; Zang, Y.; Xu, L.; Wang, J.; Jia, H.; Miao, F. Synthesis of functional conjugated microporous polymer/TiO$_2$ nanocomposites and the mechanism of the photocatalytic degradation of organic pollutants. *J. Mater. Sci.* **2021**, *56*, 7936–7950. [CrossRef]

24. Chang, C.J.; Hung, S.T. Electrochemical deposition of ZnO pore-array structures and photoconductivity of ZnO/polymer hybrid films. *Thin Solid Film.* **2008**, *517*, 1279–1283. [CrossRef]

25. Chang, C.J.; Tsai, M.H.; Hsu, Y.H.; Tuan, C.S. Morphology and optoelectronic properties of ZnO rod array/conjugated polymer hybrid films. *Thin Solid Film.* **2008**, *516*, 5523–5526. [CrossRef]

26. Jian, K.S.; Chang, C.J.; Wu, J.J.; Chang, Y.C.; Tsay, C.Y.; Chen, J.H.; Horng, T.L.; Lee, G.J.; Karuppasamy, L.; Anandan, S.; et al. High response CO sensor based on a polyaniline/SnO$_2$ nanocomposite. *Polymers* **2019**, *11*, 184. [CrossRef] [PubMed]

27. Zhu, Y.W.; Sun, Y.J.; Wang, J.L.; Yu, B.R. Antimicrobial and antifouling surfaces through polydopamine bio-inspired coating. *Rare Met.* **2021**, *40*, 1–20. [CrossRef]

28. Gao, H.; Sun, Y.; Zhou, J.; Xu, R.; Duan, H. Mussel-Inspired Synthesis of Polydopamine-Functionalized Graphene Hydrogel as Reusable Adsorbents for Water Purification. *ACS Appl. Mater. Interfaces* **2013**, *5*, 425–432. [CrossRef]

29. Zhang, C.; Yang, H.C.; Wan, L.S.; Liang, H.Q.; Li, H.; Xu, Z.K. Polydopamine-Coated Porous Substrates as a Platform for Mineralized β-FeOOH Nanorods with Photocatalysis under Sunlight. *ACS Appl. Mater. Interfaces* **2015**, *7*, 11567–11574. [CrossRef] [PubMed]

30. Liu, Y.; Ai, K.; Liu, J.; Deng, M.; He, Y.; Lu, L. Dopamine-Melanin Colloidal Nanospheres: An Efficient Near-Infrared Photothermal Therapeutic Agent for in vivo Cancer Therapy. *Adv. Mater.* **2013**, *25*, 1353–1359. [CrossRef]

31. Zhu, Z.; Su, M. Polydopamine nanoparticles for combined chemo-and photothermal cancer therapy. *Nanomaterials* **2017**, *7*, 160. [CrossRef]

32. Liu, M.; Peng, Y.; Nie, Y.; Liu, P.; Hu, S.; Ding, J.; Zhou, W. Co-delivery of doxorubicin and DNAzyme using ZnO@ polydopamine core-shell nanocomposites for chemo/gene/photothermal therapy. *Acta Biomater.* **2020**, *110*, 242–253. [CrossRef]

33. Zou, Y.; Yang, P.; Yang, L.; Li, N.; Duan, G.; Liu, X.; Li, Y. Boosting solar steam generation by photothermal enhanced polydopamine/wood composites. *Polymer* **2021**, *217*, 123464. [CrossRef]

34. Zhao, J.; Chen, J.; Chen, Z.; Zhang, Y.; Xia, D.; Wang, Q. Flexible cotton fabrics/PDA/BiOBr composite photocatalyst using bioinspired polydopamine as electron transfer mediators for dye degradation and Cr (VI) reduction under visible light. *Colloids Surf. A Physicochem. Eng. Asp.* **2020**, *593*, 124623. [CrossRef]

35. Yu, Z.; Li, F.; Yang, Q.; Shi, H.; Chen, Q.; Xu, M. Nature-mimic method to fabricate polydopamine/graphitic carbon nitride for enhancing photocatalytic degradation performance. *ACS Sustain. Chem. Eng.* **2017**, *5*, 7840–7850.

36. Nie, N.; He, F.; Zhang, L.; Cheng, B. Direct Z-scheme PDA-modified ZnO hierarchical microspheres with enhanced photocatalytic CO$_2$ reduction performance. *Appl. Surf. Sci.* **2018**, *457*, 1096–1102. [CrossRef]

37. Sun, X.; Yan, L.; Xu, R.; Xu, M.; Zhu, Y. Surface modification of TiO$_2$ with polydopamine and its effect on photocatalytic degradation mechanism. *Colloids Surf. A Physicochem. Eng. Asp.* **2019**, *570*, 199–209. [CrossRef]

38. Huang, X.; Niu, Y.; Peng, Z.; Hu, W. Core-shell structured BiOCl@polydopamine hierarchical hollow microsphere for highly efficient photocatalysis. *Colloids Surf. A Physicochem. Eng. Asp.* **2019**, *580*, 123747. [CrossRef]

39. Ding, K.; Wang, W.; Yu, D.; Gao, P.; Liu, B. Facile formation of flexible Ag/AgCl/polydopamine/cotton fabric composite photocatalysts as an efficient visible-light photocatalysts. *Appl. Surf. Sci.* **2018**, *454*, 101–111. [CrossRef]

40. Ran, J.; He, M.; Li, W.; Cheng, D.; Wang, X. Growing ZnO nanoparticles on polydopamine-templated cotton fabrics for durable antimicrobial activity and UV protection. *Polymers* **2018**, *10*, 495. [CrossRef]

41. Ran, J.; Chen, H.; Bai, X.; Bi, S.; Jiang, H.; Cai, G.; Cheng, D.; Wang, X. Immobilizing CuO/BiVO$_4$ nanocomposite on PDA-templated cotton fabric for visible light photocatalysis, antimicrobial activity and UV protection. *Appl. Surf. Sci.* **2019**, *493*, 1167–1176. [CrossRef]

42. Zhang, Y.; Yu, J.; Yu, D.; Zhou, X.; Lu, W. Enhancement in the photocatalytic and photoelectrochemical properties of visible-light driven BiVO$_4$ photocatalyst. *Rare Met.* **2011**, *30*, 192–198. [CrossRef]

43. Lai, K.; Wei, W.; Dai, Y.; Zhang, R.; Huang, B. DFT calculations on structural and electronic properties of Bi$_2$MO$_6$ (M = Cr, Mo, W). *Rare Met.* **2011**, *30*, 166–172. [CrossRef]

44. Chang, C.J.; Chao, P.Y.; Chou, C.Y.; Chen, Y.J.; Huang, C.F. Polymer/BiOBr-modified gauze as a dual-functional membrane for heavy metal removal and photocatalytic dye decolorization. *Polymers* **2020**, *12*, 2082. [CrossRef] [PubMed]

45. Zhu, D.; Zhou, Q. Novel Bi$_2$WO$_6$ modified by N-doped graphitic carbon nitride photocatalyst for efficient photocatalytic degradation of phenol under visible light. *Appl. Catal. B* **2020**, *268*, 118426. [CrossRef]

46. Wang, J.; Tang, L.; Zeng, G.; Deng, Y.; Dong, H.; Liu, Y.; Wang, L.; Peng, B.; Zhang, C.; Chen, F. 0D/2D interface engineering of carbon quantum dots modified Bi$_2$WO6 ultrathin nanosheets with enhanced photoactivity for full spectrum light utilization and mechanism insight. *Appl. Catal. B* **2018**, *222*, 115–123. [CrossRef]

47. Chang, C.J.; Chao, P.Y. Efficient photocatalytic hydrogen production by doped ZnS grown on Ni foam as porous immobilized photocatalysts. *Int. J. Hydrogen Energy* **2019**, *44*, 20805–20814. [CrossRef]

48. Chang, C.J.; Wei, Y.H.; Kuo, W.S. Free-standing CuS–ZnS decorated carbon nanotube films as immobilized photocatalysts for hydrogen production. *Int. J. Hydrogen Energy* **2019**, *44*, 30553–30562. [CrossRef]

49. Lee, S.L.; Chang, C.J. Recent progress on metal sulfide composite nanomaterials for photocatalytic hydrogen production. *Catalysts* **2019**, *9*, 457. [CrossRef]

50. Chang, C.J.; Chu, K.W. ZnS/polyaniline composites with improved dispersing stability and high photocatalytic hydrogen production activity. *Int. J. Hydrogen Energy* **2016**, *41*, 21764–21773. [CrossRef]

51. Ratova, M.; West, G.T.; Kelly, P.J. Photocatalytic visible-light active bismuth tungstate coatings deposited by reactive magnetron sputtering. *Vacuum* **2015**, *115*, 66–69. [CrossRef]

52. Xu, J.H.; Wang, W.Z.; Shang, M.; Sun, S.M.; Ren, J.; Zhang, L. Efficient visible light induced degradation of organic contaminants by Bi_2WO_6 film on SiO_2 modified reticular substrate. *Appl. Catal. B* **2010**, *93*, 227–232. [CrossRef]

53. Chang, C.J.; Chen, J.K.; Lin, K.S.; Wei, Y.H.; Chao, P.Y.; Huang, C.Y. Enhanced visible-light-driven photocatalytic degradation by metal wire-mesh supported Ag/flower-like Bi_2WO_6 photocatalysts. *J. Alloys Compd.* **2020**, *813*, 152186. [CrossRef]

54. Du, Z.; Cheng, C.; Tan, L.; Lan, J.; Jiang, S.; Zhao, L.; Guo, R. Enhanced photocatalytic activity of Bi_2WO_6/TiO_2 composite coated polyester fabric under visible light irradiation. *Appl. Surf. Sci.* **2018**, *435*, 626–634. [CrossRef]

55. Du, Z.; Guo, R.; Lan, J.; Jiang, S.; Cheng, C.; Zhao, L.; Peng, L. Preparation and photocatalytic activity of bismuth tungstate coated polyester fabric. *Fibers Polym.* **2017**, *18*, 2212–2218. [CrossRef]

56. Vautier, M.; Guillard, C.; Herrmann, J.M. Photocatalytic degradation of dyes in water: Case study of indigo and of indigo carmine. *J. Catal.* **2001**, *201*, 46–59. [CrossRef]

57. Palma-Goyes, R.E.; Silva-Agredo, J.; González, I.; Torres-Palma, R.A. Comparative degradation of indigo carmine by electrochemical oxidation and advanced oxidation processes, Electrochim. *Acta* **2014**, *140*, 427–433.

58. Silva, T.A.; Pereira, G.F.; Fatibello-Filho, O.; Eguiluz, K.I.B.; Salazar-Banda, G.R. Electroanalytical sensing of indigo carmine dye in water samples using a cathodically pretreated boron-doped diamond electrode. *J. Electroanal. Chem.* **2016**, *769*, 28–34. [CrossRef]

59. Zhang, X.; John, S. Enhanced photocatalysis by light-trapping optimization in inverse opals. *J. Mater. Chem. A* **2020**, *8*, 18974–18986. [CrossRef]

60. Chang, C.J.; Kuo, E.H. Light-trapping effects and dye adsorption of ZnO hemisphere-array surface containing growth-hindered nanorods. *Colloids Surf. A Physicochem. Eng. Asp.* **2010**, *363*, 22–29. [CrossRef]

61. Yang, J.; Wang, X.; Zhao, X.; Dai, J.; Mo, S. Synthesis of uniform Bi_2WO_6-reduced graphene oxide nanocomposites with significantly enhanced photocatalytic reduction activity. *J. Phys. Chem. C* **2015**, *119*, 3068–3078. [CrossRef]

62. Zhang, F.J.; Zhu, S.F.; Xie, F.Z.; Zhang, J.; Meng, Z.D. Plate-on-plate structured Bi_2MoO_6/Bi_2WO_6 heterojunction with high-efficiently gradient charge transfer for decolorization of MB. *Sep. Purif. Technol.* **2013**, *113*, 1–8. [CrossRef]

63. Zangmeister, R.A.; Morris, T.A.; Tarlov, M.J. Characterization of polydopamine thin films deposited at short times by autoxidation of dopamine. *Langmuir* **2013**, *29*, 8619–8628. [CrossRef] [PubMed]

64. Bernsmann, F.; Ponche, A.; Ringwald, C.; Hemmerle, J.; Raya, J.; Bechinger, B.; Voegel, J.C.; Schaaf, P.; Ball, V. Characterization of dopamine-melanin growth on silicon oxide. *J. Phys. Chem. C* **2009**, *113*, 8234–8242. [CrossRef]

65. Dreyer, D.R.; Miller, D.J.; Freeman, B.D.; Paul, D.R.; Bielawski, C.W. Elucidating the structure of poly(dopamine). *Langmuir* **2012**, *28*, 6428–6435. [CrossRef]

66. Wang, R.; Jiang, Z.; Xu, L.; Liu, C. Synthesis of Dy (III) doped Bi_2WO_6 photocatalyst with highly efficient photocatalytic performance under simulated sunlight. *J. Mater. Sci.-Mater. Electron.* **2021**, *32*, 6931–6941. [CrossRef]

67. Huang, H.; Chen, H.; Xia, Y.; Tao, X.; Gan, Y.; Weng, X.; Zhang, W. Controllable synthesis and visible-light-responsive photocatalytic activity of Bi_2WO_6 fluffy microsphere with hierarchical architecture. *J. Colloid Interface Sci.* **2012**, *370*, 132–138. [CrossRef]

68. Tejido-Rastrilla, R.; Baldi, G.; Boccaccini, A.R. Ag containing polydopamine coating on a melt-derived bioactive glass-ceramic: Effect on surface reactivity. *Ceram. Int.* **2018**, *44*, 16083–16087. [CrossRef]

69. Ku, S.H.; Lee, J.S.; Park, C.B. Spatial control of cell adhesion and patterning through mussel-inspired surface modification by polydopamine. *Langmuir* **2010**, *26*, 15104–15108. [CrossRef]

70. Shalev, T.; Gopin, A.; Bauer, M.; Stark, R.W.; Rahimipour, S. Non-leaching antimicrobial surfaces through polydopamine bio-inspired coating of quaternary ammonium salts or an ultrashort antimicrobial lipopeptide. *J. Mater. Chem.* **2012**, *22*, 2026–2032. [CrossRef]

71. Song, J.; Dai, Z.; Li, J.; Tong, X.; Zhao, H. Polydopamine-decorated boron nitride as nano-reinforcing fillers for epoxy resin with enhanced thermomechanical and tribological properties. *Mater. Res. Express* **2018**, *5*, 075029. [CrossRef]

72. Jiang, Z.; Liang, X.; Zheng, H.; Liu, Y.; Wang, Z.; Wang, P.; Zhang, X.; Qin, X.; Dai, Y.; Whangbo, M.H.; et al. Photocatalytic reduction of CO_2 to methanol by three-dimensional hollow structures of Bi_2WO_6 quantum dots. *Appl. Catal. B Environ.* **2017**, *219*, 209–215. [CrossRef]

73. Chao, P.Y.; Chang, C.J.; Lin, K.S.; Wang, C.F. Synergistic effects of morphology control and calcination on the activity of flower-like Bi_2WO_6-Bi_2O_3 photocatalysts prepared by an ionic liquid-assisted solvothermal method. *J. Alloys Compd.* **2021**, *883*, 160920. [CrossRef]

74. De Andrade, F.V.; De Lima, G.M.; Augusti, R.; Coelho, M.G.; Ardisson, J.D.; Romero, O.B. A versatile approach to treat aqueous residues of textile industry: The photocatalytic degradation of Indigo Carmine dye employing the autoclaved cellular concrete/Fe_2O_3 system. *Chem. Eng. J.* **2012**, *180*, 25–31. [CrossRef]

75. Han, D.L.; Yu, P.L.; Liu, X.M.; Xu, Y.D.; Wu, S.L. Polydopamine modified CuS@HKUST for rapid sterilization through enhanced photothermal property and photocatalytic ability. *Rare Met.* **2021**, *40*, 1–10. [CrossRef]

76. Lin, Y.; Xu, H.; Shan, X.; Di, Y.; Zhao, A.; Hu, Y.; Gan, Z. Solar steam generation based on the photothermal effect: From designs to applications, and beyond. *J. Mater. Chem. A* **2019**, *7*, 19203–19227. [CrossRef]